

Ocean deoxygenation after the Sturtian Snowball

Received: 24 August 2024

Accepted: 2 June 2025

Published online: 01 July 2025

Kun Zhang¹✉, Susan H. Little¹, Alexander J. Dickson² & Graham A. Shields¹

The abrupt ending of the Sturtian ‘Snowball’ glaciation was characterised by enhanced chemical weathering and carbon cycle perturbations, but there is less certainty over how oxygen levels responded to those changes. Here we reconcile conflicting views using a carbonate-based multiproxy dataset from the Taishir Formation in Mongolia. The geochemical data reveal an episode of ocean deoxygenation, followed by a shift toward less reducing, but still largely anoxic conditions in a post-glacial ocean characterised by nutrient and sulfate limitation. Ocean redox dynamics and biogeochemical cycling following the Sturtian deglaciation were likely dictated by unique tectonic and climatic regimes that facilitated the buildup of a recalcitrant dissolved organic carbon pool in the deep ocean. Post-glacial eutrophication may help to explain the delayed diversification of algal clades, but the persistence of ocean anoxia, excepting transient oxidation pulses, likely hindered the emergence of obligate aerobes, such as animals, until the Ediacaran Period.

The Cryogenian Period (c. 717 to 635 million years ago, or Ma) encompasses the Sturtian and Marinoan ‘Snowball Earth’ glaciations¹, together with an intervening non-glacial interlude during which a seemingly ‘normal’ hydrological cycle returned. The period represents a fundamental turning point in Earth-Life evolution, linking the ‘Tonian Transformation’² with the ‘Ediacaran-Cambrian Radiation’³. The non-glacial interlude (c. 661–650 Ma) is of particular interest due to it being a key stage in the rise toward ecosystem dominance by multicellular eukaryotes in the form of both algae and animals (putative sponges), as evidenced by organic biomarkers^{4,5}. This ecosystem reshaping was accompanied by significant perturbations to the global carbon cycle as indicated by a high carbonate carbon isotope ($\delta^{13}\text{C}_{\text{carb}}$) baseline punctuated by transient negative $\delta^{13}\text{C}_{\text{carb}}$ excursions. Examination of the Cryogenian carbon cycle has raised the hypothesis that decreased organic carbon remineralisation associated with sulfate-poor deep ocean conditions led to the growth of a large dissolved organic carbon (DOC) pool⁶, but the evidence remains controversial⁷. High $\delta^{13}\text{C}_{\text{carb}}$ values have also been related to ocean-atmosphere oxygenation, possibly caused by increased organic carbon burial and corresponding oxygen release due to a surplus of glacially induced nutrient supply, thus providing a potential link to early animal evolution⁸. Recent

studies highlight the role of uninhabitable environments for limiting animal evolution, specifically pinpointing the immediate aftermath of the Sturtian deglaciation as one such key interval^{9,10}.

Proxy evidence and modelling studies point to enhanced volcanic activity¹⁰, a brief burst of chemical weathering^{11,12} and global cooling following a super-greenhouse climate^{9,13} in the aftermath of the Sturtian deglaciation. A short-lived euxinic interval has also been inferred from iron speciation data⁹, but the underpinning mechanisms are not fully understood. Moreover, while Mo isotopes from siliciclastic deposits support extensive marine euxinia^{14,15}, this would appear to contradict U isotope records from carbonate rocks that are interpreted to indicate transient ocean oxygenation¹⁶. These conflicting views hamper our understanding of mechanistic links between climate, ocean dynamics and biological evolution during such a critical interval.

In order to resolve these uncertainties, we revisit the Taishir Formation in Mongolia, which represents one of the few continuous successions deposited on an open carbonate ramp during the non-glacial Cryogenian interval¹² (Fig. 1). Details of the geological setting are provided in the Supplementary Information. We focus on well-preserved carbonate samples from the lowermost interval of the

¹Department of Earth Sciences, University College London, London, UK. ²Centre of Climate, Ocean and Atmosphere, Department of Earth Sciences, Royal Holloway University of London, Egham, Surrey, UK. ✉e-mail: kun-zhang@ucl.ac.uk

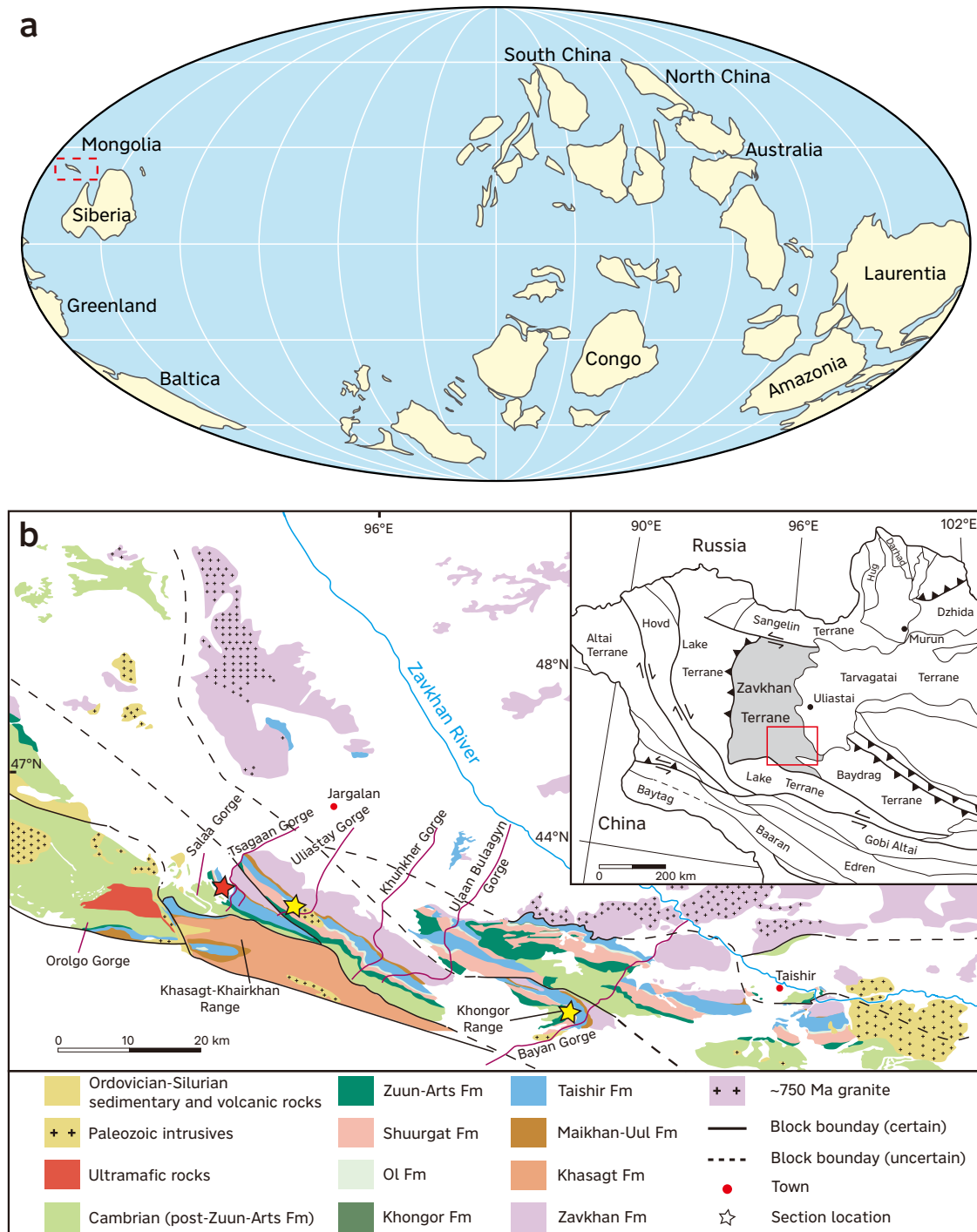


Fig. 1 | Paleogeographic and geological map of the study area. a Simplified paleogeographic reconstruction for the Cryogenian nonglacial interlude (modified after ref. 9). Dashed rectangle indicates the possible location of Mongolia from ref. 9. **b** Geological map of the Zavkhan Terrane in western Mongolia with the inset

showing tectonic terrane map of western Mongolia (modified after ref. 16 with permission from Elsevier). Fm – Formation. The studied section is denoted by the red star while previously studied sections are shown as yellow stars.

Taishir Formation, which was deposited over several million years following the Sturtian Snowball deglaciation^{11,17} (Supplementary Information). To attain insight into carbon and sulfur cycling, nutrients, weathering and marine redox conditions, we investigate a wide range of carbonate-based geochemical proxies that include carbon, sulfur, zinc, strontium and uranium isotopes, and rare earth elements (REE), phosphorus and iodine concentrations. These proxies are extracted from samples with high carbonate contents following established leaching protocols, and no significant contamination from

non-carbonate phases is identified (Methods and Supplementary Information).

One major assumption in such chemostratigraphic studies is that geochemical proxies have regional or even global significance due to the chemical and isotopic homogeneity of the world's oceans. However, transient heterogeneity may have occurred in the immediate aftermath of Cryogenian glaciations due to the abrupt release of a meltwater plume, as evidenced perhaps by the relatively radiogenic ⁸⁷Sr/⁸⁶Sr ratios of carbonates overlying Sturtian diamictites in NW

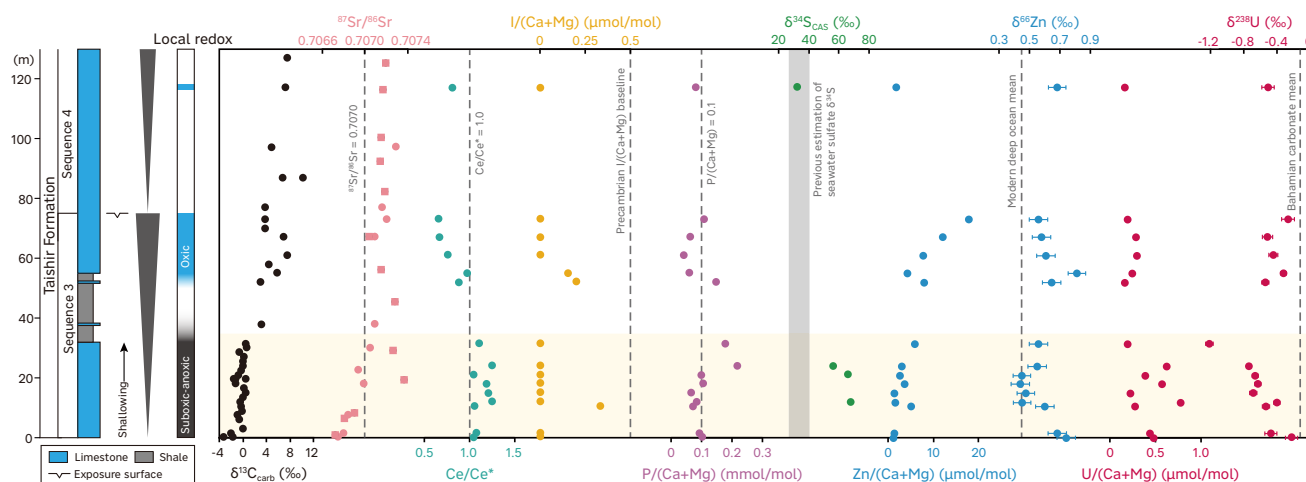


Fig. 2 | Geochemical data profiles for the studied succession from the lower part of Taishir Formation at Tsagaan Gorge. Sequence stratigraphy is from ref. 98. Lithostratigraphy, $\delta^{13}\text{C}_{\text{carb}}$ and $^{87}\text{Sr}/^{86}\text{Sr}$ data (circles) are from ref. 11. $^{87}\text{Sr}/^{86}\text{Sr}$ data (squares) of ref. 12 are correlated based on the age model of ref. 9. The Precambrian $\text{I}/(\text{Ca}+\text{Mg})$ baseline is from ref. 99. Estimation of seawater sulfate $\delta^{34}\text{S}$

is from ref. 47. The mean $\delta^{66}\text{Zn}$ value of the modern deep ocean is from ref. 53 and the mean $\delta^{238}\text{U}$ value of Bahamian carbonates is from ref. 100. The shaded band highlights the lower part of the succession. Note that $\text{I}/(\text{Ca}+\text{Mg})$ values below the detection limit are regarded as zero, and errors for some measurements of $\delta^{238}\text{U}$ are smaller than the data symbols.

Canada¹⁸. Sr isotope values in the studied interval are not anomalous but are instead consistent with the least radiogenic values from Twitya¹⁸ and Rasthof⁴⁹ carbonates. Together with the lack of typical cap carbonate sedimentary features, the studied interval seems unlikely to have been affected by a meltwater plume during deposition (Supplementary Information). Additionally, petrographic observations and critical scrutiny of diagenetic effects (Supplementary Information) show that the first-order stratigraphic trends (Fig. 2) are indicative of changes in seawater composition, and have not been significantly overprinted by diagenetic processes. Therefore, these records enable us to depict a more holistic picture of post-Sturtian environments and interrogate potential links between environmental change and biological evolution during the rise to organic complexity.

Results and discussion

Local redox conditions

Cerium anomalies archived in carbonate rocks can provide insights into local water column redox conditions, whereby negative Ce anomalies (values below 0.9–1), accompanied by seawater-like REE patterns, are commonly considered to indicate oxic conditions^{20,21}. Samples with seawater-like REE patterns in this study show average Ce anomalies of 1.11 and 0.78 for the lower (0–32 m) and upper (50–120 m) parts of the succession, respectively. While we observed non-seawater-like REE patterns from the lower part (Supplementary Fig. 6; Supplementary Information), the exclusion of these values does not affect the overall Ce anomaly trend, which is consistent with previous studies^{11,16} (Fig. 2). This indicates that the depositional settings transitioned from largely suboxic/anoxic seafloor conditions²⁰ during deposition of the lower part, to oxic conditions for the upper part. The very low sulfur contents in decarbonated residues of the samples¹¹ further indicate that the local seawater and/or pore water was mostly non-sulfidic during deposition of the lower part.

Carbonate-associated iodine, expressed as $\text{I}/(\text{Ca}+\text{Mg})$, is emerging as another useful proxy for tracking shallow seawater redox conditions²². This is mainly because only iodate is incorporated into carbonates²³, is prevalent in oxic seawater and reduces rapidly to iodide in low-oxygen environments²⁴. Owing to the relatively slow oxidation kinetics of iodide^{25,26}, carbonate $\text{I}/(\text{Ca}+\text{Mg})$ ratios are also sensitive to oxycline proximity^{27,28}. The low $\text{I}/(\text{Ca}+\text{Mg})$ values ($< 0.5 \mu\text{mol/mol}$) in our samples are consistent with most Proterozoic carbonate records (Fig. 2), which have been interpreted to indicate a

redox-stratified water column with a shallow oxycline²⁹. Nevertheless, $\text{I}/(\text{Ca}+\text{Mg})$ is highly susceptible to diagenesis³⁰ and generally decreases during diagenetic alteration²⁹. Considering that the samples may have experienced neomorphism, diagenetic iodine loss cannot be ruled out entirely (Supplementary Information).

Transient ocean deoxygenation

The sulfur isotope composition of carbonate-associated sulfate ($\delta^{34}\text{S}_{\text{CAS}}$) is a useful tool for reconstructing the dynamic sulfur cycle, which is linked to Earth's surface oxidation state through pyrite burial³¹. Recent advances in geochemical redox proxies have also allowed the extent of global seafloor anoxia to be estimated by uranium isotopes in carbonate rocks^{16,32,33}. In short, during the reduction of soluble U(VI) to particulate-reactive U(IV), heavy ^{238}U is favoured due to the nuclear field shift effect³⁴. Intensified U(IV) removal to sediments during periods of expanded marine anoxia thus drives seawater $\delta^{238}\text{U}$ toward lower values. Although there appears to be some effect from organic matter loading on uranium isotope fractionation³⁵, large isotopic fractionation is generally associated with uranium reduction. Therefore, marine anoxia is considered to exert a dominant control on the seawater $\delta^{238}\text{U}$.

Our carbonate $\delta^{238}\text{U}$ values (Fig. 2), combined with published $\delta^{238}\text{U}$ records¹⁶ from different stratigraphic sections, reveal a decreasing trend following the Sturtian deglaciation (Fig. 3). The decreasing trend cannot readily be explained by sea-level changes or chemical weathering (Supplementary Information) and instead suggests significant expansion of anoxic waters. This evidence for expanded anoxia is accompanied by extremely high $\delta^{34}\text{S}_{\text{CAS}}$ values (mean 63‰; Supplementary Information), which require enhanced microbial sulfate reduction and removal of ^{32}S -enriched pyrite from the ocean³⁶. Therefore, the $\delta^{238}\text{U}$ and $\delta^{34}\text{S}_{\text{CAS}}$ data together suggest greatly expanded marine anoxia and pyrite burial following the Sturtian deglaciation. Indeed, coupled high $\delta^{34}\text{S}_{\text{CAS}}$ ($> +40\text{‰}$) and low $\delta^{238}\text{U}$ ($< -1\text{‰}$) values are also evident during the late Ediacaran^{32,33,36,37} and similarly attributed to the spread of euxinic seawater and enhanced pyrite burial, along with an elevated isotopic ratio of sulfur input ($\delta^{34}\text{S}_{\text{in}}$)^{33,36–38}. This coupling may also explain the observed trend following the Sturtian deglaciation, as glacial erosion could have exposed Tonian evaporites leading to elevated $\delta^{34}\text{S}_{\text{in}}$, while the expansion of euxinic seawater is further supported by iron speciation records⁹ (Fig. 3).

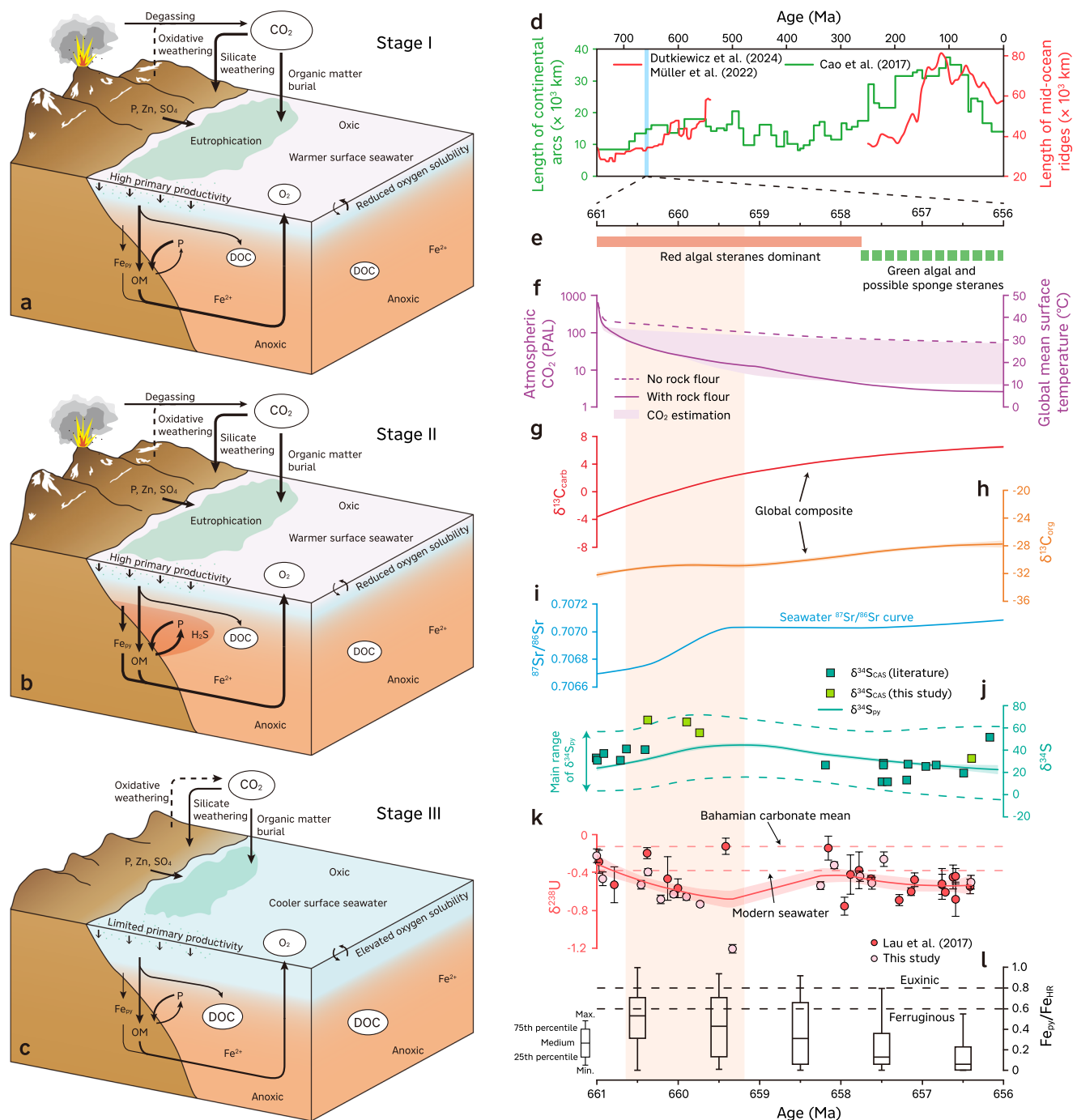


Fig. 3 | Conceptual model and biogeochemical indicators following the Sturtian deglaciation. **a** Vigorous weathering induced eutrophication after the Sturtian deglaciation. **b** Expansion of euxinia on productive margins owing to excess of H_2S over iron. **c** Continuous atmospheric CO_2 drawdown led to subdued weathering, cooling and shallow seawater oxygenation. In (a–c), the thicknesses of arrows indicate the relative magnitude of fluxes, and the sizes of ellipses represent the relative sizes of reservoirs. **d** Global length of continental arcs⁷⁴ and mid-ocean ridges^{75,101}. The blue band indicates the studied interval. **e** Occurrences of biomarkers⁹. **f** Possible evolution of atmospheric CO_2 and global mean surface temperature⁹. **g–i** Compilation of carbon, strontium, sulfur, uranium isotopes and

iron speciation records (modified after ref. 9). Solid lines in (g, h, j, k) represent the LOESS (locally estimated scatterplot smoothing) fitting curves, and the shaded area represents 1σ (68%) confidence interval. The dashed lines in (j) indicate the major range of $\delta^{34}\text{S}_{\text{py}}$. In (l), each boxplot represents the distribution of global $\text{Fe}_{\text{py}}/\text{Fe}_{\text{HR}}$ data in each one-million-year time bin. The light shade of pale red band indicates the second stage. The age model of (e–l) is based on model A of ref. 9 (see Supplementary Fig. 2 for the alternative age model D). OM organic matter burial, Fe_{py} pyrite burial, DOC dissolved organic carbon pool, PAL present atmospheric level, Min. minimum, Max. maximum.

The integrated carbonate $\delta^{238}\text{U}$ records then show a shift towards relatively higher values with a mean of -0.49‰ (Fig. 3). This $\delta^{238}\text{U}$ value has been associated with the post-Sturtian ocean oxygenation, with -0.5‰ of the seafloor being anoxic compared to -0.2‰ in the modern ocean^{16,39}. Alternatively, this $\delta^{238}\text{U}$ value is similar to that of most mid-

Proterozoic carbonates, which has been interpreted to indicate limited euxinia in an ocean that was still largely anoxic⁴⁰. Such a discrepancy is related to limited U isotope fractionation under suboxic and ferruginous conditions^{41,42}. Recent studies suggest that U isotope fractionation associated with ferruginous conditions may vary significantly,

the magnitude of which is possibly linked to primary productivity with limited $\delta^{238}\text{U}$ fractionation under the low-productivity, ferruginous environment^{43–45}. Given the potentially decreased primary productivity⁴⁶ (see also the following discussion), we consider that the positive $\delta^{238}\text{U}$ shift, instead of indicating widespread oxygenation, is more likely to reflect the return to less reducing conditions with a concomitant reduction in marine euxinia. The inference of a reduction in marine euxinia is in accordance with low $\delta^{98}\text{Mo}$ values in coeval shales^{14,15} and decreasing $\delta^{34}\text{S}_{\text{CAS}}$ and pyrite $\delta^{34}\text{S}$ ($\delta^{34}\text{S}_{\text{py}}$) values (Fig. 3), which in turn implies an increase in sulfate levels¹⁰. Nevertheless, seawater sulfate concentrations overall remained reasonably low as evidenced by low $\Delta^{34}\text{S}$ ($\delta^{34}\text{S}_{\text{CAS}} - \delta^{34}\text{S}_{\text{py}}$) values^{47,48} and low [CAS] in these samples (see Methods and Supplementary Data) and coeval carbonates⁴⁸. Taken together, integrating $\delta^{238}\text{U}$ and $\delta^{34}\text{S}$ evidence suggests that the post-Sturtian ocean experienced a transient ocean deoxygenation marked by the expansion of low-sulfate euxinic seawater, followed by a return to less reducing conditions.

Nutrient dynamics

Zinc is a bioessential micronutrient that functions as a cofactor in important enzymes such as carbonic anhydrase and alkaline phosphatase. The use of Zn isotopes to trace perturbations to micronutrient cycling is relatively new^{49–52}, but builds on extensive investigation of Zn isotope systematics. The modern deep ocean is mostly homogeneous with respect to $\delta^{66}\text{Zn}$ at around +0.45‰⁵³, which is isotopically heavier than riverine input (−0.33‰)^{54,55}. Euxinic sediments could potentially record seawater $\delta^{66}\text{Zn}$ due to near quantitative removal of Zn^{56,57}. Carbonate rocks are estimated to represent a minor sink for Zn^{54,58}. Biogenic carbonates such as corals appear to be able to record the seawater $\delta^{66}\text{Zn}$ value⁵⁹, yet inorganic carbonates are isotopically heavier than the deep ocean with an offset of around 0.4‰ potentially due to Zn²⁺ incorporation through tetrahedral coordination^{58,60,61}. While Fe–Mn crusts and nodules are 0.4–0.5‰ heavier than seawater^{54,55}, recent studies suggest that the quantitatively most important oxic sink is dominated by pelagic oxic sediments⁶², which is 0.1–0.2‰ lighter than seawater^{58,63}. Importantly, the only significant sink of isotopically light Zn in largely anoxic oceans seems to be organic-rich continental margin sediments⁶⁴. In light of this global Zn isotope mass balance framework, past variations in seawater Zn isotope compositions as recorded in carbonate rocks and/or shales have been used to infer changes in Zn input to, and output from the ocean^{49–52}.

Carbonate $\delta^{66}\text{Zn}$ values exhibit a shift from +0.74‰ to +0.45‰, and remain around +0.45‰ in the lower part of the succession, followed by a gradual increase upsection to +0.68‰ (Fig. 2). The relatively low background $\delta^{66}\text{Zn}$ values compared to modern carbonates⁶¹ might relate to the largely diminished pelagic oxic sink in deep ferruginous oceans. The $\delta^{66}\text{Zn}$ stratigraphic variation is unlikely to be accounted for by changes in relative sea-level and/or local redox conditions (Supplementary Information). Instead, considering the isotopic offset between carbonates and seawater, $\delta^{66}\text{Zn}$ variation in the lower part suggests a shift towards low regional seawater $\delta^{66}\text{Zn}$ values. This negative shift broadly coincides with the prominent rise of $^{87}\text{Sr}/^{86}\text{Sr}$ indicating significantly elevated weathering rates¹¹ (Fig. 2). Hence, one possible explanation is that strong postglacial weathering delivered abundant light Zn from continents either due to enhanced deglacial volcanism¹⁰ and/or exposed large igneous provinces⁹. Shifts to lower seawater $\delta^{66}\text{Zn}$ values have also been attributed to a diminished light Zn sink (i.e., removal into organic-rich sediments) compensated for by expanded euxinic⁵⁰ or oxic (Fe–Mn crusts/nodules)⁵² sinks, or to enhanced isotopically light Zn input from benthic^{52,53} or hydrothermal⁵³ sources. A strong direct influence of hydrothermal Zn seems unlikely given the insignificant carbonate Eu anomalies in samples (−1.0), while increasing $^{87}\text{Sr}/^{86}\text{Sr}$ values are also inconsistent with a more globally significant hydrothermal source. Considering the U and S isotope evidence for expanding anoxia/euxinia during

deposition of the lower part, any increased oxic sink (Fe–Mn crusts/nodules) or benthic input due to oxygenation can also be largely excluded. An increased euxinic sink alone would lead to a decrease in the marine Zn reservoir and hence carbonate Zn concentrations⁵⁰, but Zn/(Ca+Mg) shows a consistent increasing trend in the lower part (Fig. 2). The relatively stable $\delta^{66}\text{Zn}$ during the expansion of anoxia/euxinia as indicated by $\delta^{238}\text{U}$ and $\delta^{34}\text{S}$ records (Fig. 2) also suggests that an expanded euxinic sink is unlikely to give rise to $\delta^{66}\text{Zn}$ variability in the lower part. On the other hand, the $\delta^{66}\text{Zn}$ values then gradually increase upsection, and its onset occurs prior to the shift to less reducing conditions as indicated by Ce/Ce* and U isotopes (Fig. 2), implying a limited role for an expanding oxic sink. Furthermore, the transition to less reducing conditions in the upper part may have decreased seawater $\delta^{66}\text{Zn}$ values via remobilization of light Zn from continental margin sediments⁵². Considering the coincidence with the plateauing of $^{87}\text{Sr}/^{86}\text{Sr}$ ratios, the increase in $\delta^{66}\text{Zn}$ suggests that weathering-derived light Zn input was progressively outweighed by a relative increase in the burial of isotopically light organic-rich sediments. Overall, $\delta^{66}\text{Zn}$ evidence suggests an enhanced nutrient supply into the ocean following the Sturtian deglaciation likely leading to eutrophication, followed by a period of diminished influx.

Phosphorus is considered to be the ultimate limiting nutrient for primary productivity in oceans over geological timescales⁶⁵. Carbonate P/(Ca+Mg) can record relative changes to oceanic phosphate levels in deep time as long as other potential influences can be deconvolved^{66,67}. The lower part of the succession has a relatively higher mean P/(Ca+Mg) (0.11 mmol/mol) ratio with a prominent peak to 0.2 mmol/mol near its top, compared to the upper part (mean 0.08 mmol/mol) (Fig. 2). The partitioning of phosphate into carbonate minerals is affected by the fluid phosphate concentration, pH, temperature, alkalinity, mineralogy and precipitation rates⁶⁸. Following the post-Sturtian super-greenhouse climate, the oceans could have received enhanced alkalinity and calcium input from weathering¹³, which might have increased carbonate precipitation rates⁶⁸. Meanwhile, there seem to be no significant variations in ocean pH⁶⁹ and mineralogy (Supplementary Information). The combined effects would likely decrease carbonate P/(Ca+Mg) values, and hence, the prominent peak in the lower part implies relatively elevated seawater phosphate levels. Because of the nutrient-type distribution of dissolved phosphate in the ocean, shallow seawater would be expected to exhibit phosphate depletion, making the prominent increase with basin shallowing even more remarkable. The peak of P/(Ca+Mg) broadly coincides with high $\delta^{34}\text{S}_{\text{CAS}}$ and low $\delta^{238}\text{U}$ values, suggesting that the increase in dissolved phosphate concentrations resulted from low P burial efficiency due to intensified recycling under euxinic/sulfidic conditions⁷⁰. This positive nutrient recycling feedback is also supported by phosphorus phase association and iron speciation records from coeval strata⁹.

Weathering induced biogeochemical cascades

Redox dynamics and the global carbon cycle following the Sturtian deglaciation were dictated by an extreme climatic, but also a highly unusual tectonic regime (Fig. 3). Specifically, the peneplanation of Rodinia after its amalgamation⁷¹ likely led to a relatively low-relief supercontinent, on which chemical weathering was more transport- than rate-limited. During the long-lasting Sturtian glaciation, ice sheets scoured these relatively flat-lying continental interiors, removing regolith and surface rocks, and producing highly reactive rock flour^{6,72}. As a consequence, the high $p\text{CO}_2$ levels accumulated during glaciation decreased rapidly after deglaciation due to enhanced silicate weathering^{13,72} but were not readily replenished due to unusually low arc volcanism^{73,74} and mid-ocean ridge carbon outflux⁷⁵ (Fig. 3). The brief episode of intense chemical weathering that followed deglaciation led therefore into a more prolonged interval of global cooling, in accordance with the temporal evolution of seawater $^{87}\text{Sr}/^{86}\text{Sr}$ (Fig. 3), and markedly lower nutrient and sulfate delivery to the ocean^{46,72}.

The ocean at the end of the Sturtian deglaciation (~661 Ma) was probably dominated by anoxic ferruginous conditions (Fig. 3a) with euxinia delayed by limited sulfate availability in the oceans and a high proportional influx of iron relative to sulfate⁶. With increasing nutrient and sulfate input, a tipping point must have been crossed whereby a relative excess of H₂S over iron promoted the expansion of euxinia. Enhanced P recycling under euxinic/sulfidic conditions in turn exerted a positive productivity feedback^{9,70} (Fig. 3b). Consequently, elevated organic carbon and pyrite burial, as evidenced by a coupled increase in $\delta^{13}\text{C}_{\text{carb}}$ and $\delta^{34}\text{S}$, would have resulted in a pulse of oxygen production. However, stimulated primary production would also have increased organic export to the deep ocean, increasing the oxygen demand for organic matter remineralisation⁷⁶. The overall low seawater sulfate levels may also have increased the seabed methane flux, helping to keep seafloors anoxic⁷⁷. Hence, increased oxygen consumption in the marine realm associated with organic matter (and possibly methane) oxidation resulted in ocean deoxygenation.

Following the eutrophication episode, the gradual decrease in weathering-derived nutrient and sulfate influx led to a lessening of marine euxinia⁹, in part due to a negative productivity feedback caused by less efficient P recycling (Fig. 3c). Together with increased oxygen solubility driven by a cooling climate⁷⁸, this change would have been conducive to the expansion of less reducing environments in the marine realm. The cooling climate could also have decreased microbial respiration and hence induced a more efficient biological carbon pump⁷⁹. In the absence of abundant oxidants, this process may have favoured organic matter preservation as supported by increasing $\delta^{13}\text{C}_{\text{carb}}$ (Fig. 3). Nonetheless, $\delta^{34}\text{S}$ records broadly show an inverse relationship with $\delta^{13}\text{C}_{\text{carb}}$ during this stage (Fig. 3). Such a decoupling appears to suggest that the oxidant (oxygen) generated by organic carbon burial was partly transferred into sulfate through a surplus of pyrite weathering over burial, thereby limiting the extent of atmospheric oxygenation. Collectively, the above scenarios illustrate that oxygenation of the atmosphere and oceans (especially the deep marine realm) was likely asynchronous during the Cryogenian nonglacial interlude.

Implications for the carbon cycle and biological evolution

Sustained high $\delta^{13}\text{C}_{\text{carb}}$ values during the Cryogenian nonglacial interlude are conventionally interpreted to infer elevated organic carbon burial rates⁸. We suggest that the redox and nutrient dynamics, as discussed earlier, should also have enlarged the marine DOC inventory and hence impacted the carbon cycle. During post-glacial eutrophication, abundant organic substrates were available but would not have been efficiently degraded under expanded anoxia conditions, thus promoting DOC accumulation⁸⁰. The later nutrient-limited condition, in conjunction with decreased microbial respiration driven by a cooling climate, would also have limited microbial DOC consumption^{81–83}. Therefore, post-Sturtian environmental change led to the net accumulation of a recalcitrant DOC pool in the deep ocean, which is supported by a relatively muted $\delta^{13}\text{C}_{\text{org}}$ shift compared with the prominent rise of $\delta^{13}\text{C}_{\text{carb}}$ (Fig. 3). The DOC pool could have switched from net accumulation to net oxidation once certain oxidant thresholds were crossed, buffering against extensive oceanic oxygenation and atmospheric CO₂ drawdown^{78,84}. Such a prediction is consistent with coincident negative shifts of both $\delta^{238}\text{U}$ and $\delta^{13}\text{C}_{\text{carb}}$ through the Taishir anomaly¹⁶. Taken together, we suggest that the sustained high $\delta^{13}\text{C}_{\text{carb}}$ following the Sturtian Snowball deglaciation is at least in part due to the buildup of a deep ocean DOC pool.

Marine anoxia and high sea surface temperatures have been invoked to explain the delayed rise of green algae and putative demosponges after the Sturtian deglaciation^{5,9,10}. There is a broad coincidence between the development of less reducing environments, cooling climate and the rise of biotic complexity (Fig. 3). A synergistic effect can be envisioned whereby a lessening of marine anoxia alongside limited nutrient availability and moderate climate would have extended

the habitable space, perhaps setting the stage for the expansion of opportunistic species. Therefore, our dataset appears to support the idea that severe environmental stress after the Sturtian deglaciation delayed further biological diversification. Nonetheless, conditions would have been favourable only to aerobic forms with low oxygen demands because the oceans were still not significantly oxygenated. Later oceans remained largely anoxic and the episodic transitions towards a more oxygenated system throughout the late Neoproterozoic appear to have relied on external stimuli such as tectonic drivers. This reliance may explain the prolonged rise of oxygen and delayed occurrence of energetic lifestyles over the late Ediacaran to Cambrian.

Methods

Bulk limestone samples were crushed into small rock chips. The clean chips without visible veins and weathered surfaces were selected and ground into fine powders using a TEMA agate disc mill or agate mortar and pestle for further processing.

Rare earth elements and phosphorus

Rare earth elements (REE) and phosphorus were extracted using sequential leaching⁸⁵. For each sample, ~50 mg powder was prewashed with 5 ml neutral 1 M ammonium acetate. The mixture was sonicated in the ultrasonic bath for 30 min and then centrifuged for 5 min, from which the supernatants were discarded. The residues were rinsed with de-ionized (DI) water (18.2 M Ω -cm) three times, followed by partial leaching with dilute acetic acid (0.3 M) for 30 min in the ultrasonic bath. The resultant supernatants obtained by centrifugation were filtered into acid cleaned Teflon beakers using 0.22 μm syringe filters, dried on a hot plate and redissolved in 2% HNO₃. The solutions were further diluted in 2% HNO₃ for major and minor element analysis (Ca, Mg, Fe, Mn, Al, P, Sr, Ba) on a Varian 720 inductively coupled plasma optical emission spectrometer (ICP-OES) at University College London. Phosphorus was analysed at a wavelength of 213.618 nm using the polyboost function. The leachates were then diluted to ~100 ppm Ca with 2% HNO₃ for rare earth elements analysis via an Agilent 7900 inductively coupled plasma mass spectrometer (ICP-MS) at University College London. The internal standard of 2 ppb indium was added to all analysed solutions to monitor the instrumental drift and matrix effects. The formation of 2+ ions and oxide interference were monitored using Ba²⁺ and the formation rate of Ce oxide before analysis. Correction of BaO interference on Eu was achieved by monitoring single Ba elemental solutions throughout the analytical session. The accuracy was monitored by two in-house bulk digested solution standards of SRM-88a and SGR-1, which showed agreeable values with certified values within uncertainty. Repeated analysis of the drift monitor and standards gave a precision better than 5%. Blanks showed negligible concentrations below the detection limit. REE concentrations are normalised against post-Archean Australian Shale⁸⁶ (denoted by the subscript N). The bell-shaped index (BSI) is calculated after ref. 87 to evaluate the enrichment of middle REE. The Ce anomaly is calculated following ref. 88 $\text{Ce}/\text{Ce}^* = \text{Ce}_N \times \text{Nd}_N / \text{Pr}_N^2$.

Carbonate-associated iodine

The carbonate-associated iodine (CAI) was extracted according to an updated method⁸⁹. Around 10 mg powder was sonicated in 1 ml DI water that was then centrifuged and discarded. The residue was leached with 1 ml 3% HNO₃ in the ultrasonic bath for 10 min. After centrifugation, an aliquot of the supernatant was pipetted into the stabiliser (3% ethylenediaminetetraacetic acid in 3% ammonium hydroxide). Such stock solution was then diluted in the stabiliser for Ca and Mg analysis using a Varian 720 ICP-OES at University College London. The accuracy was checked with two in-house solution standards of SRM-88a and SGR-1, and blanks were negligible. Based on the results, the stock solution was further diluted to ~100 ppm Ca with the stabiliser for iodine analysis on an Agilent 7900 ICP-MS at University

College London. Calibration standards were made freshly from potassium iodate powder, dissolved in the stabiliser with 100 ppm Ca matched to samples. The detection limit of I/Ca is $\sim 0.1 \mu\text{mol/mol}$. Repeated analysis of the drift monitor gave the relative standard deviation better than 3%. Analyses of JCP-1 and CRM-393 duplicates yielded I/Ca values of $3.90 \pm 0.04 \mu\text{mol/mol}$ (1 SD, $n = 3$) and $0.39 \mu\text{mol/mol} \pm 0.001$ (1 SD, $n = 3$), which were comparable to published literature values^{22,89}. The stabilisers and procedure blanks showed negligible iodine concentrations.

Carbonate-associated sulfate

Approximately 15–30 g of sample powder was first immersed in excess 12% NaClO followed by ultrasonication in a water bath for 1 h and shaken overnight. The residues after centrifugation were rinsed with DI water three times. The bleaching process was repeated five times, after which the residues were saturated in excess 1% H_2O_2 overnight under constant agitation. The residues were rinsed with DI water three times and dried out in the oven. The dried residues were cleaned with excess 10% NaCl for 24 h on an orbital shaker and then rinsed with DI water three times. The cleaning process was repeated five times, after which the residues were dissolved in 6 M HCl within 45 min. The leachates were filtered through 0.22 μm syringe filters immediately, to which a 200 g/L BaCl_2 solution was added to precipitate BaSO_4 . The resultant precipitates were washed with 6 M HCl once and DI water three times before being dried and weighed for sulfur isotope analysis. This multistep process for carbonate-associated sulfate (CAS) extraction follows the method of ref. 90 to minimise any potential contamination from non-carbonate phase sulfur. No precipitate was observed from the blank. Sulfur isotope analysis of dried precipitates ($\delta^{34}\text{S}_{\text{CAS}}$) was carried out at Iso-Analytical Laboratory (UK) using the EA-IRMS. The sample and vanadium pentoxide catalyst contained in a tin capsule were combusted at 1080 °C in the presence of oxygen, which was further combusted by passing through tungstic oxide/zirconium oxide in a helium stream, followed by reduction by high purity copper wires. Water is removed using a Nafion™ membrane, while SO_2 is resolved from N_2 and CO_2 on a packed gas chromatograph column at a temperature of 45 °C before it was introduced into the IRMS. The analysis was based on monitoring of m/z 48, 49 and 50 of SO^+ produced from SO_2 , and $\delta^{34}\text{S}$ values are reported relative to the Vienna Canon Diablo Troilite (VCDT) standard. Three lab working standards (IA-R025, IA-R026, IA-R061) were used for calibration, which have been analysed against the international standards NBS-127 (+20.3‰), IAEA-SO-5 (+0.5‰) and IAEA-S-1 (−0.3‰). The accuracy was monitored by analysing IA-R061 ($+20.51\text{‰} \pm 0.11$, 1 s.d., $n = 3$) and IAEA-SO-5 ($+0.71\text{‰} \pm 0.03$, 1 s.d., $n = 2$), which are consistent with reported values. The CAS concentrations were calculated based on the weights of dried precipitates and the sample purity determined during sulfur isotope analysis. It should be noted that while we processed all the samples, only five samples yield sufficient sulfur for isotopic analyses.

Uranium isotopes

Approximately 500 mg sample powder was partially leached with 20 ml 0.2 M acetic acid for 24 h at room temperature in order to limit the contamination of uranium associated with non-carbonate phases⁹¹. Following centrifugation, the supernatants were filtered through 0.22 μm syringe filters, aliquoted and diluted for measurement of elemental concentrations (Ca, Mg, Fe, Mn, Al, Sr, U) using ICP-OES and ICP-MS at University College London. The accuracy was assessed by the analysis of in-house solution standards of TMDA-70, SGR-1, and SRM-88a, which were in agreement with certified values. Repeated analysis of the drift monitor gave the relative standard deviation better than 5%. Based on measured U concentrations, around 40 ng U was pipetted into acid-cleaned Teflon beakers and mixed with IRMM 3636 uranium double spike to achieve a spike/sample ratio of approximately 0.1. The mixtures were dried down and

redissolved in 1 ml 3 M HNO_3 . Uranium was then purified using Eichrom UTEVA resin following the protocol of ref. 92. Briefly, columns and resin were cleaned with 0.05 M HCl and conditioned with 3 M HNO_3 before loading samples. The matrix elements and Th were eluted using 3 M HNO_3 and 6 M HCl, respectively, and U was collected with 0.05 M HCl. Purified samples were oxidised with concentrated HNO_3 and redissolved in 3% HNO_3 before analysis at Royal Holloway University of London. Uranium isotope ratios were measured on a Thermo-Finnigan Neptune Plus multi-collector inductively coupled plasma mass spectrometer (MC-ICP-MS) equipped with an Aridus III desolvating nebulizer system for sample introduction. Acid blank was analysed before every solution analysis to correct measured intensities. Uranium isotope ratios are reported relative to CRM-112A standard:

$$\delta^{238}\text{U} = \left[\left(\frac{{}^{238}\text{U}/{}^{235}\text{U}_{\text{sample}}}{({}^{238}\text{U}/{}^{235}\text{U}_{\text{CRM-112A}})} - 1 \right) \right] \times 1000$$

Propagated analytical uncertainties for individual $\delta^{238}\text{U}$ measurements were typically 0.03–0.08‰ (2 SE) for ~ 15 ppb solutions. A limestone standard CRM-393 was processed in the same manner as samples and gave a $\delta^{238}\text{U}$ of $-0.35 \pm 0.08\text{‰}$ (2 SE), which agrees with known values. Two duplicates were processed through the same full procedure and showed excellent agreement. Total procedural blank was ~ 5 pg of U and negligible. The error is reported as propagated uncertainty on individual isotope ratios.

Zinc isotopes

Carbonate-bound zinc was extracted following the protocol of ref. 61. Around 200 mg of sample powder was rinsed with DI water three times, then leached with 20 ml buffered 1 M ammonium acetate solution (pH 5) for 24 h at room temperature under constant agitation. The supernatants after centrifugation were pipetted into new acid-cleaned tubes. The aliquots of leachates were diluted in 2% HNO_3 for elemental analysis (Ca, Mg, Fe, Mn, Al, Sr, Zn) using ICP-OES and ICP-MS at University College London. The in-house solution standards of TMDA-70, SGR-1, and SRM-88a were analysed to check the accuracy, which exhibited values consistent with certified values. Repeated analysis of the drift monitor gave the relative standard deviation better than 5%. Based on the Zn concentrations, 100–200 ng Zn was pipetted into acid-cleaned Teflon beakers, which were dried down on the hotplate, oxidised with excess concentrated HNO_3 and refluxed with 1 ml 6 M HCl. The certain amount of a ${}^{64}\text{Zn}$ - ${}^{67}\text{Zn}$ double spike was added to all samples to achieve a spike/sample ratio of approximately ~ 1.1 – 1.2 ⁹³, followed by evaporation to dryness and refluxed with 1 ml 6 M HCl. Solutions were further dried down and redissolved in 1 ml 1 M HCl to ensure spike-sample equilibration. Zinc was then purified through column chromatography using AG MP-1M resin (BioRad) following refs. 54,94. In brief, columns and resin were cleaned with 2% HNO_3 and conditioned with 1 M HCl before loading samples. The matrix elements were eluted with 1 M HCl, and Zn was collected with 0.01 M HCl. Prior to analysis, purified samples were oxidised with concentrated HNO_3 and redissolved in 2% HNO_3 . Zinc isotopes were measured on a Nu Instruments Plasma 3 MC-ICP-MS at University College London following the protocol of refs. 59,93,95. Solutions of ~ 100 ppb Zn were introduced via an Aridus III desolvating nebulizer system and a PFA nebulizer (50 $\mu\text{L/min}$). A standard-sample bracketing approach was adopted during analysis, and the raw data collection was preceded by an analysis of 2% HNO_3 for signal correction. Interference corrections for ${}^{64}\text{Ni}$ and Ba^{2+} were negligible. Instrumental mass bias was corrected through the double-spike technique⁹³ using the off-line data reduction procedure of ref. 96. Zinc isotope ratios were determined relative to a new standard AA-ETH Zn:

$$\delta^{66}\text{Zn} = \left[\left(\frac{{}^{66}\text{Zn}/{}^{64}\text{Zn}_{\text{sample}}}{({}^{66}\text{Zn}/{}^{64}\text{Zn}_{\text{AA-ETH}})} - 1 \right) \right] \times 1000$$

Final $\delta^{66}\text{Zn}$ values are reported with respect to JMC-Lyon by applying a correction of $+0.28\text{‰}$ ⁹⁷. Total procedural blanks were $\sim 1\text{--}2\text{ ng}$. Accuracy and external reproducibility of $\delta^{66}\text{Zn}$ values were assessed by two secondary solution standards (London Zn and NCS DC70303) and a limestone standard (CRM-393) that was processed through the same full procedure as the samples. Solution standards gave a $\delta^{66}\text{Zn}$ of $0.11 \pm 0.04\text{‰}$ (2 SD, $n = 14$) for London Zn and a $\delta^{66}\text{Zn}$ of $0.73 \pm 0.06\text{‰}$ (2 SD, $n = 6$) for NCS DC70303, which are consistent with previously reported values⁵⁹. CRM-393 gave a $\delta^{66}\text{Zn}$ of $0.75 \pm 0.05\text{‰}$ (2 SD, $n = 4$). Three duplicates were processed along with samples to assess internal reproducibility and yielded agreeable values within the error of uncertainty. The reported error on figures is the external 2 SD reproducibility of NCS DC70303, which was the largest external uncertainty during the measurement period.

Ethics and inclusion

We affirm that all geological materials were collected in a responsible manner and in accordance with relevant permits and local laws. Local and regional research relevant to this study has been cited where appropriate.

Data availability

The original data generated in this study are provided in the Supplementary Information and deposited in the Figshare repository (<https://doi.org/10.6084/m9.figshare.29135669>).

References

- Hoffman, P. F. et al. Snowball Earth climate dynamics and Cryogenian geology-geobiology. *Sci. Adv.* **3**, e1600983 (2017).
- Brocks, J. J. et al. Lost world of complex life and the late rise of the eukaryotic crown. *Nature* **618**, 767–773 (2023).
- Wood, R. et al. Integrated records of environmental change and evolution challenge the Cambrian Explosion. *Nat. Ecol. Evol.* **3**, 528–538 (2019).
- Love, G. D. et al. Fossil steroids record the appearance of Demospongiae during the Cryogenian period. *Nature* **457**, 718–721 (2009).
- Brocks, J. J. et al. The rise of algae in Cryogenian oceans and the emergence of animals. *Nature* **548**, 578–581 (2017).
- Swanson-Hysell, N. L. et al. Cryogenian Glaciation and the Onset of Carbon-Isotope Decoupling. *Science* **328**, 608–611 (2010).
- Johnston, D. T., Macdonald, F. A., Gill, B. C., Hoffman, P. F. & Schrag, D. P. Uncovering the Neoproterozoic carbon cycle. *Nature* **483**, 320–323 (2012).
- Planavsky, N. J. et al. The evolution of the marine phosphate reservoir. *Nature* **467**, 1088–1090 (2010).
- Bowyer, F. T. et al. Biological diversification linked to environmental stabilization following the Sturtian Snowball glaciation. *Sci. Adv.* **9**, eadf9999 (2023).
- Li, M. et al. Deglacial volcanism and reoxygenation in the aftermath of the Sturtian Snowball Earth. *Sci. Adv.* **9**, eadh9502 (2023).
- Shields, G. A., Brasier, M. D., Stille, P. & Dorjnamjaa, D. Factors contributing to high $\delta^{13}\text{C}$ values in Cryogenian limestones of western Mongolia. *Earth Planet. Sci. Lett.* **196**, 99–111 (2002).
- Bold, U. et al. Neoproterozoic stratigraphy of the Zavkhan terrane of Mongolia: The backbone for Cryogenian and early Ediacaran chemostratigraphic records. *Am. J. Sci.* **316**, 1–63 (2016).
- Le Hir, G. et al. The snowball Earth aftermath: Exploring the limits of continental weathering processes. *Earth Planet. Sci. Lett.* **277**, 453–463 (2009).
- Scheller, E. L. et al. Ocean redox conditions between the snowballs – Geochemical constraints from Arena Formation, East Greenland. *Precambrian Res.* **319**, 173–186 (2018).
- Cheng, M. et al. Delayed Neoproterozoic oceanic oxygenation: Evidence from Mo isotopes of the Cryogenian Datangpo Formation. *Precambrian Res.* **319**, 187–197 (2018).
- Lau, K. V., Macdonald, F. A., Maher, K. & Payne, J. L. Uranium isotope evidence for temporary ocean oxygenation in the aftermath of the Sturtian Snowball Earth. *Earth Planet. Sci. Lett.* **458**, 282–292 (2017).
- Shields, G., Stille, P., Brasier, M. D. & Atudorei, N. Stratified oceans and oxygenation of the late Precambrian environment: a post glacial geochemical record from the Neoproterozoic of W. Mongolia. *Terra Nov.* **9**, 218–222 (1997).
- Rooney, A. D. et al. Re-Os geochronology and coupled Os-Sr isotope constraints on the Sturtian snowball Earth. *Proc. Natl Acad. Sci. USA* **111**, 51–56 (2014).
- Yoshioka, H., Asahara, Y., Tojo, B. & Kawakami, S. ichi. Systematic variations in C, O, and Sr isotopes and elemental concentrations in neoproterozoic carbonates in Namibia: Implications for a glacial to interglacial transition. *Precambrian Res.* **124**, 69–85 (2003).
- Tostevin, R. et al. Low-oxygen waters limited habitable space for early animals. *Nat. Commun.* **7**, 12818 (2016).
- Zhang, K. & Shields, G. A. Sedimentary Ce anomalies: Secular change and implications for paleoenvironmental evolution. *Earth-Sci. Rev.* **229**, 104015 (2022).
- Lu, Z., Lu, W., Rickaby, R. E. M. & Thomas, E. *Earth History of Oxygen and the iprOxy. Earth History of Oxygen and the iprOxy* vol. 6454 (Cambridge University Press, 2020).
- Lu, Z., Jenkyns, H. C. & Rickaby, R. E. M. Iodine to calcium ratios in marine carbonate as a paleo-redox proxy during oceanic anoxic events. *Geology* **38**, 1107–1110 (2010).
- Wong, G. T. F. & Brewer, P. G. The marine chemistry of iodine in anoxic basins. *Geochim. Cosmochim. Acta* **41**, 151–159 (1977).
- Chance, R., Baker, A. R., Carpenter, L. & Jickells, T. D. The distribution of iodide at the sea surface. *Environ. Sci. Process. Impacts* **16**, 1841–1859 (2014).
- Hardisty, D. S. et al. Limited iodate reduction in shipboard seawater incubations from the Eastern Tropical North Pacific oxygen deficient zone. *Earth Planet. Sci. Lett.* **554**, 116676 (2021).
- Lu, Z. et al. Oxygen depletion recorded in upper waters of the glacial Southern Ocean. *Nat. Commun.* **7**, 11146 (2016).
- Lu, W. et al. Late inception of a resiliently oxygenated upper ocean. *Science* **177**, 174–177 (2018).
- Hardisty, D. S. et al. Perspectives on Proterozoic surface ocean redox from iodine contents in ancient and recent carbonate. *Earth Planet. Sci. Lett.* **463**, 159–170 (2017).
- Lau, K. V. & Hardisty, D. S. Modeling the impacts of diagenesis on carbonate paleoredox proxies. *Geochim. Cosmochim. Acta* **337**, 123–139 (2022).
- Fike, D. A., Bradley, A. S. & Rose, C. V. Rethinking the ancient sulfur cycle. *Annu. Rev. Earth Planet. Sci.* **43**, 593–622 (2015).
- Zhang, F. et al. Extensive marine anoxia during the terminal Ediacaran Period. *Sci. Adv.* **4**, 1–12 (2018).
- Tostevin, R. et al. Uranium isotope evidence for an expansion of anoxia in terminal Ediacaran oceans. *Earth Planet. Sci. Lett.* **506**, 104–112 (2019).
- Andersen, M. B., Stirling, C. H. & Weyer, S. Uranium isotope fractionation. *Rev. Mineral. Geochem.* **82**, 799–850 (2017).
- Lau, K. V., Lyons, T. W. & Maher, K. Uranium reduction and isotopic fractionation in reducing sediments: Insights from reactive transport modeling. *Geochim. Cosmochim. Acta* **287**, 65–92 (2020).
- Fike, D. A. & Grotzinger, J. P. A paired sulfate-pyrite $\delta^{34}\text{S}$ approach to understanding the evolution of the Ediacaran-Cambrian sulfur cycle. *Geochim. Cosmochim. Acta* **72**, 2636–2648 (2008).
- Tostevin, R. et al. Constraints on the late Ediacaran sulfur cycle from carbonate associated sulfate. *Precambrian Res.* **290**, 113–125 (2017).

38. Clarkson, M. O. et al. Environmental controls on very high $\delta^{238}\text{U}$ values in reducing sediments: Implications for Neoproterozoic seawater records. *Earth-Sci. Rev.* **237**, 104306 (2023).
39. Kipp, M. A. & Tissot, F. L. H. Inverse methods for consistent quantification of seafloor anoxia using uranium isotope data from marine sediments. *Earth Planet. Sci. Lett.* **577**, 117240 (2022).
40. Gilleaudeau, G. J. et al. Uranium isotope evidence for limited euxinia in mid-Proterozoic oceans. *Earth Planet. Sci. Lett.* **521**, 150–157 (2019).
41. Cole, D. B. et al. Uranium Isotope Fractionation in Non-sulfidic Anoxic Settings and the Global Uranium Isotope Mass Balance. *Glob. Biogeochem. Cycles* **34**, 0–2 (2020).
42. Bruggmann, S. et al. Uranium isotope cycling on the highly productive Peruvian margin. *Chem. Geol.* **590**, 120705 (2022).
43. Lau, K. V. et al. Variable local basin hydrography and productivity control the uranium isotope paleoredox proxy in anoxic black shales. *Geochim. Cosmochim. Acta* **317**, 433–456 (2022).
44. Rutledge, R. L. et al. Productivity and organic carbon loading control uranium isotope behavior in ancient reducing settings: Implications for the paleoredox proxy. *Geochim. Cosmochim. Acta* **368**, 197–213 (2024).
45. Gilleaudeau, G. J. et al. Uranium isotope systematics of a low-productivity ferruginous ocean analog: Implications for the uranium isotope record of early Earth. *Geochim. Cosmochim. Acta* **392**, 195–206 (2025).
46. Fru, E. C. et al. Transient fertilization of a post-Sturtian Snowball ocean margin with dissolved phosphate by clay minerals. *Nat. Commun.* **14**, 8418 (2023).
47. Wang, P. et al. Large accumulations of ^{34}S -enriched pyrite in a low-sulfate marine basin: The Sturtian Nanhua Basin, South China. *Precambrian Res.* **335**, 105504 (2019).
48. Hurtgen, M. T., Arthur, M. A., Suits, N. S. & Kaufman, A. J. The sulfur isotopic composition of Neoproterozoic seawater sulfate: Implications for a snowball Earth?. *Earth Planet. Sci. Lett.* **203**, 413–429 (2002).
49. Kunzmann, M. et al. Zn isotope evidence for immediate resumption of primary productivity after snowball Earth. *Geology* **41**, 27–30 (2013).
50. John, S. G., Kunzmann, M., Townsend, E. J. & Rosenberg, A. D. Zinc and cadmium stable isotopes in the geological record: A case study from the post-snowball Earth Nuccaleena cap dolostone. *Palaeogeogr. Palaeoclimatol. Palaeoecol.* **466**, 202–208 (2017).
51. Liu, S. A. et al. Zinc isotope evidence for intensive magmatism immediately before the end-Permian mass extinction. *Geology* **45**, 343–346 (2017).
52. Sweere, T. C., Dickson, A. J., Jenkyns, H. C., Porcelli, D. & Henderson, G. M. Zinc- and cadmium-isotope evidence for redox-driven perturbations to global micronutrient cycles during Oceanic Anoxic Event 2 (Late Cretaceous). *Earth Planet. Sci. Lett.* **546**, 116427 (2020).
53. Lemaitre, N. et al. Pervasive sources of isotopically light zinc in the North Atlantic Ocean. *Earth Planet. Sci. Lett.* **539**, 116216 (2020).
54. Little, S. H., Vance, D., Walker-Brown, C. & Landing, W. M. The oceanic mass balance of copper and zinc isotopes, investigated by analysis of their inputs, and outputs to ferromanganese oxide sediments. *Geochim. Cosmochim. Acta* **125**, 673–693 (2014).
55. Moynier, F., Vance, D., Fujii, T. & Savage, P. The Isotope Geochemistry of Zinc and Copper. *Rev. Mineral. Geochem.* **82**, 543–600 (2017).
56. Vance, D. et al. The oceanic budgets of nickel and zinc isotopes: the importance of sulfidic environments as illustrated by the Black Sea. *Philos. Trans. R. Soc. A Math. Phys. Eng. Sci.* **374**, 20150294 (2016).
57. Isson, T. T. et al. Tracking the rise of eukaryotes to ecological dominance with zinc isotopes. *Geobiology* **16**, 341–352 (2018).
58. Dickson, A. J. The zinc isotope composition of late Holocene open-ocean marine sediments. *Chem. Geol.* **605**, 120971 (2022).
59. Little, S. H. et al. Cold-water corals as archives of seawater Zn and Cu isotopes. *Chem. Geol.* **578**, (2021).
60. Mavromatis, V., González, A. G., Dietzel, M. & Schott, J. Zinc isotope fractionation during the inorganic precipitation of calcite – Towards a new pH proxy. *Geochim. Cosmochim. Acta* **244**, 99–112 (2019).
61. Müsing, K., Clarkson, M. O. & Vance, D. The meaning of carbonate Zn isotope records: Constraints from a detailed geochemical and isotope study of bulk deep-sea carbonates. *Geochim. Cosmochim. Acta* **324**, 26–43 (2022).
62. Little, S. H., de Souza, G. F. & Xie, R. C. Metal stable isotopes in the marine realm. in *Treatise on Geochemistry* 285–332 (Elsevier, 2025). <https://doi.org/10.1016/B978-0-323-99762-1.00019-X>.
63. Zhang, G. et al. Balancing the oceanic Zn isotope budget: The key role of deep-sea pelagic sediments. *Geology* **XX**, 1–5 (2024).
64. Little, S. H., Vance, D., McManus, J. & Severmann, S. Key role of continental margin sediments in the oceanic mass balance of Zn and Zn isotopes. *Geology* **44**, 207–210 (2016).
65. Tyrrell, T. The relative influences of nitrogen and phosphorus on oceanic primary production. *Nature* **400**, 525–531 (1999).
66. Dodd, M. S. et al. Development of carbonate-associated phosphate (CAP) as a proxy for reconstructing ancient ocean phosphate levels. *Geochim. Cosmochim. Acta* **301**, 48–69 (2021).
67. Ingalls, M., Grotzinger, J. P., Present, T., Rasmussen, B. & Fischer, W. W. Carbonate-Associated Phosphate (CAP) Indicates Elevated Phosphate Availability in Neoproterozoic Shallow Marine Environments. *Geophys. Res. Lett.* **49**, e2022GL098100 (2022).
68. Dodd, M. S. et al. Uncovering the Ediacaran phosphorus cycle. *Nature* **618**, 974–980 (2023).
69. Kasemann, S. A., Prave, A. R., Fallick, A. E., Hawkesworth, C. J. & Hoffmann, K. H. Neoproterozoic ice ages, boron isotopes, and ocean acidification: Implications for a snowball Earth. *Geology* **38**, 775–778 (2010).
70. Xiong, Y. et al. Phosphorus cycling in Lake Cadagno, Switzerland: A low sulfate euxinic ocean analogue. *Geochim. Cosmochim. Acta* **251**, 116–135 (2019).
71. Spencer, C. J. et al. Proterozoic onset of crustal reworking and collisional tectonics: Reappraisal of the zircon oxygen isotope record. *Geology* **42**, 451–454 (2014).
72. Mills, B., Watson, A. J., Goldblatt, C., Boyle, R. & Lenton, T. M. Timing of Neoproterozoic glaciations linked to transport-limited global weathering. *Nat. Geosci.* **4**, 861–864 (2011).
73. McKenzie, N. R. et al. Continental arc volcanism as the principal driver of icehouse-greenhouse variability. *Science* **352**, 444–447 (2016).
74. Cao, W., Lee, C. T. A. & Lackey, J. S. Episodic nature of continental arc activity since 750 Ma: A global compilation. *Earth Planet. Sci. Lett.* **461**, 85–95 (2017).
75. Dutkiewicz, A. et al. Duration of Sturtian “Snowball Earth” glaciation linked to exceptionally low mid-ocean ridge outgassing. *Geology* **52**, 292–296 (2024).
76. Lenton, T. M. & Daines, S. J. Biogeochemical Transformations in the History of the Ocean. *Ann. Rev. Mar. Sci.* **9**, 31–58 (2017).
77. He, T. et al. An enormous sulfur isotope excursion indicates marine anoxia during the end-Triassic mass extinction. *Sci. Adv.* **6**, eabb6704 (2020).
78. Peltier, W. R., Liu, Y. & Crowley, J. W. Snowball Earth prevention by dissolved organic carbon remineralization. *Nature* **450**, 813–818 (2007).
79. Boscolo-Galazzo, F. et al. Temperature controls carbon cycling and biological evolution in the ocean twilight zone. *Science* **371**, 1148–1152 (2021).

80. Jiao, N. et al. The microbial carbon pump and climate change. *Nat. Rev. Microbiol.* **22**, 408–419 (2024).
81. Lennartz, S. T., Keller, D. P., Oschlies, A., Blasius, B. & Dittmar, T. Mechanisms Underpinning the Net Removal Rates of Dissolved Organic Carbon in the Global Ocean. *Global Biogeochem. Cycles* **38**, e2023GB007912 (2024).
82. Roshan, S. & DeVries, T. Efficient dissolved organic carbon production and export in the oligotrophic ocean. *Nat. Commun.* **8**, 2036 (2017).
83. Fakhraee, M., Tarhan, L. G., Planavsky, N. J. & Reinhard, C. T. A largely invariant marine dissolved organic carbon reservoir across Earth's history. *Proc. Natl. Acad. Sci. USA* **118**, e2103511118 (2021).
84. Shields, G. A. et al. Unique Neoproterozoic carbon isotope excursions sustained by coupled evaporite dissolution and pyrite burial. *Nat. Geosci.* **12**, 823–827 (2019).
85. Zhang, K. & Shields, G. A. Early diagenetic mobilization of rare earth elements and implications for the Ce anomaly as a redox proxy. *Chem. Geol.* **635**, 121619 (2023).
86. McLennan, S. M. Chapter 7. Rare earth elements in sedimentary rocks: influence of provenance and sedimentary processes. in *Geochemistry and Mineralogy of Rare Earth Elements* 169–200 (De Gruyter, 1989). <https://doi.org/10.1515/9781501509032-010>.
87. Tostevin, R. et al. Effective use of cerium anomalies as a redox proxy in carbonate-dominated marine settings. *Chem. Geol.* **438**, 146–162 (2016).
88. Lawrence, M. G. & Kamber, B. S. The behaviour of the rare earth elements during estuarine mixing-revisited. *Mar. Chem.* **100**, 147–161 (2006).
89. Zhang, K., Tarbuck, G. & Shields, G. A. Refining the carbonate-associated iodine redox proxy with leaching experiments. *Chem. Geol.* **646**, 121896 (2024).
90. Tian, Z., Zhou, Y. & Shields, G. A. Experimental comparisons of carbonate-associated sulfate extraction methods. *EarthArxiv* (2022) <https://doi.org/10.31223/X56S87>.
91. Dahl, T. W. et al. Atmosphere-ocean oxygen and productivity dynamics during early animal radiations. *Proc. Natl. Acad. Sci. USA* **116**, 19352–19361 (2019).
92. Basu, A., Sanford, R. A., Johnson, T. M., Lundstrom, C. C. & Löffler, F. E. Uranium isotopic fractionation factors during U(VI) reduction by bacterial isolates. *Geochim. Cosmochim. Acta* **136**, 100–113 (2014).
93. Arnold, T. et al. Measurement of zinc stable isotope ratios in biogeochemical matrices by double-spike MC-ICPMS and determination of the isotope ratio pool available for plants from soil. *Anal. Bioanal. Chem.* **398**, 3115–3125 (2010).
94. Archer, C. & Vance, D. Mass discrimination correction in multiple-collector plasma source mass spectrometry: An example using Cu and Zn isotopes. *J. Anal. Spectrom.* **19**, 656–665 (2004).
95. Little, S. H. et al. Cu and Zn isotope fractionation during extreme chemical weathering. *Geochim. Cosmochim. Acta* **263**, 85–107 (2019).
96. Siebert, C., Nägler, T. F. & Kramers, J. D. Determination of molybdenum isotope fractionation by double-spike multicollector inductively coupled plasma mass spectrometry. *Geochem., Geophys. Geosystems* **2**, 1032 (2001).
97. Archer, C. et al. Inter-calibration of a proposed new primary reference standard AA-ETH Zn for zinc isotopic analysis. *J. Anal. Spectrom.* **32**, 415–419 (2017).
98. Lindsay, J. F. et al. Facies and sequence controls on the appearance of the Cambrian biota in southwestern Mongolia: Implications for the Precambrian-Cambrian boundary. *Geol. Mag.* **133**, 417–428 (1996).
99. Lu, W. et al. Iodine proxy evidence for increased ocean oxygenation during the Bitter Springs Anomaly. *Geochemical Perspect. Lett.* **5**, 53–57 (2017).
100. Chen, X. et al. Diagenetic effects on uranium isotope fractionation in carbonate sediments from the Bahamas. *Geochim. Cosmochim. Acta* **237**, 294–311 (2018).
101. Müller, R. D. et al. Evolution of Earth's tectonic carbon conveyor belt. *Nature* **605**, 629–639 (2022).

Acknowledgements

We would like to thank E.E. Stüeken and Xi Chen for insightful discussions; Zheyu Tian and Lin Yuan for help with experiments; A. Basu and G. Tarbuck for technical support. K.Z. was financially supported by the China Scholarship Council, University College London Faculty Dean's Prize and International Association of Sedimentologists (IAS) Post-graduate Research Grant. G.S. acknowledges funding support from the joint NERC-NSFC Biosphere Evolution Transitions and Resilience (BETR) programme NE/P013643/1 and NERC project NE/R010129/1. G.S. gratefully acknowledges the financial support of the John Templeton Foundation (#62220). The opinions expressed in this paper are those of the authors and not those of the John Templeton Foundation.

Author contributions

G.A.S. and K.Z. conceived the study; G.A.S. supervised the project; S.H.L., A.J.D. and K.Z. contributed to the generation of geochemical data; K.Z. wrote the initial draft of the manuscript. All authors contributed to reviewing and editing the manuscript at all stages.

Competing interests

The authors declare no competing interests.

Additional information

Supplementary information The online version contains supplementary material available at <https://doi.org/10.1038/s41467-025-60700-w>.

Correspondence and requests for materials should be addressed to Kun Zhang.

Peer review information *Nature Communications* thanks the anonymous reviewers for their contribution to the peer review of this work. A peer review file is available.

Reprints and permissions information is available at <http://www.nature.com/reprints>

Publisher's note Springer Nature remains neutral with regard to jurisdictional claims in published maps and institutional affiliations.

Open Access This article is licensed under a Creative Commons Attribution 4.0 International License, which permits use, sharing, adaptation, distribution and reproduction in any medium or format, as long as you give appropriate credit to the original author(s) and the source, provide a link to the Creative Commons licence, and indicate if changes were made. The images or other third party material in this article are included in the article's Creative Commons licence, unless indicated otherwise in a credit line to the material. If material is not included in the article's Creative Commons licence and your intended use is not permitted by statutory regulation or exceeds the permitted use, you will need to obtain permission directly from the copyright holder. To view a copy of this licence, visit <http://creativecommons.org/licenses/by/4.0/>.

© The Author(s) 2025